Biomech Model Mechanobiol
DOI 10.1007/s10237-015-0675-z

ORIGINAL PAPER

Characterization of the three-dimensional kinematic behavior of axons in central nervous system white matter

Sagar Singh[1] · **Assimina A. Pelegri**[2] · **David I. Shreiber**[1]

Received: 21 November 2014 / Accepted: 2 April 2015

Abstract Traumatic injury to axons in white matter of the brain and spinal cord occurs primarily via tensile stretch. During injury, the stress and strain experienced at the tissue level is transferred to the microscopic axons. How this transfer occurs, and the primary constituents dictating this transfer must be better understood to develop more accurate multi-scale models of injury. Previous studies have characterized axon tortuosity and kinematic behavior in 2-dimensions (2-D), where axons have been modeled to exhibit non-affine (discrete), affine (composite-like), or switching behavior. In this study, we characterize axon tortuosity and model axon kinematic behavior in 3-dimensions (3-D). Embryonic chick spinal cords at different development stages were excised and stretched. Cords were then fixed, transversely sectioned, stained, and imaged. 3-D axon tortuosity was measured from confocal images using a custom-built MATLAB script. 2-D kinematic models previously described in Bain et al. (J Biomech Eng 125(6):798, 2003) were extended, re-derived, and validated for the 3-D case. Results showed that 3-D tortuosity decreased with stretch, exhibiting similar trends with changes in development as observed in the 2-D studies. Kinematic parameters also displayed similar general trends. Axons demonstrated more affine behavior with increasing stretch and development. In comparison with 2-D results, a smaller percentage of the populations of 3-D axons were predicted to follow pure non-affine behavior. The data and kinematic models presented herein can be incorporated into multi-scale CNS injury models, which can advance the accuracy of the models and improve the potential to identify axonal injury thresholds.

Keywords Axon · Brain injury · Axonal injury · White matter · Multi-scale model

1 Introduction

Axonal injury is a proximal cause of functional deficits following central nervous system (CNS) trauma and is most often caused by excessive tensile strain (Smith and Meaney 2000). During trauma, strain is transferred from the tissue scale to individual axons. Within CNS white matter, although axons are predominantly oriented, they are not perfectly straight, but instead follow an undulated, tortuous path (Bain et al. 2003). This tortuosity, which we define as the ratio of the path length to the end-to-end length of an axon, affects the transfer of strain from the macroscale to the microscale. Axon tortuosity has been characterized in 2-dimensions (2-D) in chick embryo spinal cord white matter (Hao and Shreiber 2007) and in guinea pig optic nerves (Bain et al. 2003) in control tissue and tissue exposed to stretch in situ.

As can be expected, when excised white matter tissue is stretched, axons become progressively straighter and axon tortuosity decreases. However, the manner in which axons straighten and subsequently experience tension is non-uniform and dependent on the tissue-level stretch (Bain et al. 2003; Hao and Shreiber 2007). Generally, the constituents of composite/composite-like materials, such as white matter, can demonstrate different degrees of kinematic coupling to the other constituents. In non-affine kinematic models of white matter, for instance, axons are assumed to be fully

✉ David I. Shreiber
shreiber@rci.rutgers.edu

[1] Department of Biomedical Engineering, Rutgers, The State University of New Jersey, 599 Taylor Road, Piscataway, NJ 08854, USA

[2] Department of Mechanical and Aerospace Engineering, Rutgers, The State University of New Jersey, 98 Brett Road, Piscataway, NJ 08854, USA

Published online: 25 April 2015

uncoupled and straighten independently of one another with a given macroscopic stretch. Conversely, in affine modes, axons are fully coupled to the surrounding matrix and stretch together with tissue-level stretch, resulting in continuum-like behavior. Previous studies of 2-D axon kinematics demonstrated that axons present a combination of the two types of behavior. As stretch is initiated, axons first behave non-affinely, but switch to affine-like behavior with increasing stretch. Bain et al. hypothesized that the transition was due to coupling to the glial matrix of myelinating oligodendrocytes (Bain et al. 2003). This hypothesis was strengthened by results that demonstrated a clear shift toward more affine behavior with increasing myelination in a chick embryo spinal cord model, and by a characterization of the tensile properties of myelinated and experimentally de-myelinated spinal cords (Hao and Shreiber 2007; Shreiber et al. 2009).

Of course, axons traverse a 3-dimensional (3-D) path, and although we hypothesize that the kinematics will follow the same trends as in 2-D, the degree of tortuosity and characteristics of the transition from non-affine to affine kinematics may differ substantially. Previous studies have attempted to model the axon in 3-D, either as a fascicle of hexagonally arranged straight cylinders (Bas and Erdogmus 2010), or as a helical coil (Nilsson et al. 2012), though neither study explored microstructure behavior due to stretch. Karami et al. used finite element modeling to simulate axon kinematics due to tissue-level stretch (Karami et al. 2009). However, the study relied on 2-D tortuosity and kinematic data to generate 3-D predictions and assumed pure affine behavior. More recently, Pan et al. (2013) modeled axons in a "pseudo 3-D" representative volume element (RVEs) that incorporated 2-D coupling behavior (Pan et al. 2013). However, model predictions have not been validated in 3-D. Characterizing and modeling axon kinematics in 3-D will improve the predictive capabilities of CNS primary injury models, particularly in predicting axonal injury strain thresholds. In this work, we experimentally characterize axon tortuosity in 3-D in the embryonic chick spinal cord as a function of tissue-level stretch. We then extend the model developed by Bain et al. (2003) and fitting procedures used in our previous study (Hao and Shreiber 2007) to describe axon kinematic behavior in 3-D. We hypothesize that axon tortuosity in 3-D will be greater than 2-D, but that kinematic changes with development will be similar.

2 Methods

2.1 Chick embryo spinal cord isolation

Fresh fertile chicken eggs (Charles River Laboratories North Franklin, CT) were incubated to specific development stages (Embryonic Day (E)—E12, E14, E16, and E18). The intact spinal cord was excised by cutting along the length of the spinal column and removing the dorsal portion of the vertebrae. The full length of the spinal cord from the first cervical vertebrae (C1) to the eleventh lumbar vertebrae (L11) was measured three times with digital calipers and averaged. A piece of reflective plastic (glitter) was carefully placed onto the cord at the C3, C8, T4, and L4 regions. The distance between glitter markers was measured in situ, and the ventral portions of the vertebrae were removed. The spinal cord was pinned on each end of a custom-built microstretch device composed of two rapid-prototype platforms and immersed in 37 °C saline. The distances between the glitter markers were measured three times and averaged. The spinal cord was stretched back to its in situ length and was then quasistatically stretched to a stretch ratio (λ) of 1 (unstretched control), 1.05, 1.10, 1.15, or 1.2 defined as:

$$\lambda = \frac{\text{Final length of spinal cord}}{\text{Initial length of spinal cord}}$$

After stretching, spinal cords were photographed, and the distances between plastic markers were measured in their stretched state to confirm uniformity. Saline was replaced with 4 % paraformaldehyde to fix the tissue in the stretched state. Previous studies demonstrated that fixation did not affect the undulation or morphological appearance of axons in the spinal cord (Bain et al. 2003). Spinal cords were fixed in their stretched state for 15 min, carefully removed from the device, and re-measured to ensure length did not change during fixation. Spinal cords were stored in 4 % paraformaldehyde overnight at 4 °C, and then transferred to a cryoprotectant 20 % sucrose-saline solution for at least 24 h before sectioning and staining.

2.2 Immunohistochemistry

Spinal cords were removed from cryoprotectant solution and divided into cervical, thoracic, and lumbar regions with a razor blade. Each of these sections was divided again for longitudinal (Fig. 1a) or transverse (Fig. 1b) sectioning. Regions were embedded in O.C.T. compound (Electron Microscopy Services). Frozen transverse or longitudinal sections (30 µm thick) were cut on a cryostat (Thermo Electron) and placed on pre-treated glass slides (Fisher). Transverse sections were used for imaging in 3-D. Longitudinal sections were used to image the 2-D tortuosity for measuring by hand to validate our image processing algorithm (described below) and directly compare 2-D tortuosity measurements to our previous study (Hao and Shreiber 2007). Sections were rinsed four times in immunobuffer (1 % bovine serum albumin, and 0.5 % Triton X-100 in phosphate buffered saline) for 5 min each, and then incubated in a 10 % goat serum blocking buffer for 1 h. Sections were incubated overnight at 4 °C with a

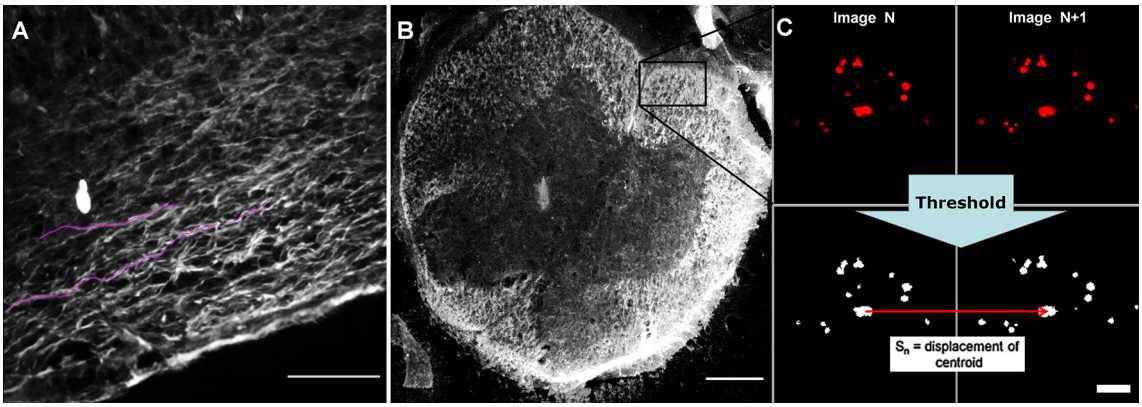

Fig. 1 **a** Longitudinal sections of spinal cord tissue were stained for neurofilament-200 kD to track 2-D tortuosity. These results were then compared with the x–z and y–z results from our custom-built image processing algorithm for validation (*scale bar* = 100 μm). **b** Transverse sections were stained for neurofilament-200 kD and MBP (*scale bar* = 200 μm). The composite images showed the tell-tale "butterfly" signifying the location of white matter in spinal cords. **c** Zoomed-in white matter region of the cross section. Images confocally taken with ×100 oil immersion objective were thresholded. Displacement of each axon's centroid (S_n) was then summed through the image stack to calculate axon path length and tortuosity. (*scale bar* = 2 μm)

primary antibody mixture of a 1:1000 dilution of mouse monoclonal α-Neurofilament-200 (Sigma) and a 1:500 dilution of rat monoclonal α-Myelin Basic Protein (MBP) (Invitrogen). Sections were again washed with immunobuffer four times for 15 min each and then incubated in a 1:400 dilution of Alexa 568 goat-anti-mouse secondary antibody and a 1:400 dilution of Alexa 488 goat-anti-rat secondary antibody for 1 h. Sections were washed a final time with immunobuffer four more times for 15 min each and allowed to air-dry in the dark. Slides were then coverslipped with mounting solution (Vector Labs).

2.3 Histology

To quantify the degree of myelination, three spinal cords from each stage of development were fixed and stained with osmium tetroxide (OsO_4, Electron Microscopy Services). Stained spinal cords were embedded in epoxy resin, sectioned into 1-μm thick slices with a microtome, counterstained with toluidine blue, and coverslipped.

2.4 Imaging

Confocal images of immunostained spinal cord sections were captured with an Olympus IX81 inverted epifluorescent microscope equipped with a spinning disk confocal unit and a Hamamatsu ImagEM digital camera (Middlesex NJ). Images were taken at 100× with filters at 488 nm and at 568 nm to visualize the different secondary antibody labeling ("Appendix" Fig. 5 for Representative Image). Images of 100 optical sections at increments of 0.3 μm were captured through the thickness of each slice. Both the ventral funiculus and lateral funiculus were selected for imaging. Immunolabeling was observed to be qualitatively the most consistent in the ventral funiculus. The lateral funiculus was also imaged to provide side-by-side comparison with our previous study (Hao and Shreiber 2007).

For longitudinal sections, the paths of 20–40 axons per image were traced using ImageJ. Tortuosity in 2-D was calculated by dividing the path length of the tracing by the end-to-end length. To examine the degree of myelination, osmium tetroxide-stained cross sections were imaged using a 100× oil immersion objective under brightfield. Myelination was quantified by counting the number of myelinated fibers in images of each region. G-ratio was calculated for each myelinated axon and was defined as the ratio of inner axonal diameter to outer diameter for each myelinated fiber (Chomiak and Hu 2009).

2.5 Image processing for 3-D tortuosity extraction

Image stacks were processed using a custom MATLAB script. Localized thresholding within an image was accomplished by dividing each image into a grid of 64 × 64 pixel subregions and operating on each subregion separately. The median intensity in each subregion was used as the threshold intensity. The processed regions were stitched back together to reconstruct the full image. The centroids of individual axons were identified in the first image of the stack. A 50 × 50 pixel region around each axon was cropped. Using a nearest neighbors approach, the next image of the stack was processed within the same 50 × 50 pixel region, and the Euclidian distance of the axon's centroid between the two images was calculated (Fig. 1c). If more than one axon was

present in the search area, the axon with the smallest distance was considered the correct one. This process was repeated for each image in the stack, and the centerpoint displacements were stored and summed to determine the total path length that the axon has traveled. The tortuosity of the axon was then calculated.

This process was repeated for each axon in the original image. Histograms of 3-D axon tortuosity were produced for each stretch level and development stage. Histograms for 2-D axon tortuosity for x–z and y–z longitudinal planes were also produced. The automated tracking algorithm was validated against 2-D and 3-D tortuosities measured by hand.

2.6 Mathematical model

Axon kinematics were modeled with MATLAB scripts modified from our previous study (Hao and Shreiber 2007) that predicted tortuosity distributions at various stretch levels in the pure affine or non-affine states. The experimental distributions were first compared to idealized non-affine and affine distributions. The 3-D tortuosity data for unstretched specimens were used as input for the scripts. Expressions for the dependence of tortuosity on tissue-level stretch ratio (λ) in 3-D were derived for non-affine and affine states.

2.6.1 Non-affine model

When non-affine kinematics are assumed, axons will straighten according to the level of tissue-scale stretch. When the stretch level reaches the initial tortuosity, the axon is assumed to be perfectly straight and maintains a tortuosity value of 1 thereafter.

$$T_{3D} = \frac{1}{\lambda} T_0 \quad \text{for } \lambda < T_0 \tag{1}$$

$$T_{3D} = 1 \quad \text{for } \lambda \geq T_0 \tag{2}$$

2.6.2 Affine model

In affine behavior, axons are assumed to be interconnected with each other via the glial matrix, such that individual axons experience the same geometric transformations as the macroscopic tissue. A 3-D axon was modeled as a helical coil, using two parametric periodic functions to describe the axon's path in each plane (x–z and y–z planes). The tortuosity for a fully coupled axon can be calculated by:

$$T_{3D} = T_0 \sqrt{\left\{ \frac{1}{\lambda^{8/3}} + \frac{1}{T_0^2} \left[1 - \frac{2\pi}{(2\pi + k^2)\lambda^{8/3}} \left(\frac{1}{k^2} + \frac{1}{2\pi} \right) \right] \right\}} \tag{3}$$

where k corresponds to the cross-ratio of amplitude and periodicity in the x–z and y–z planes (i.e., $A_{xz}/P_{yz} = A_{yz}/P_{xz}$). Based on observations from unstretched spinal cords, which indicated that the amplitude and periodicity are similar in each plane, k was set to one. A derivation for (3) is provided in the "Appendix".

2.6.3 Switching model

In the switching model, axons initially follow non-affine kinematics and transition to affine behavior at specific tortuosities uniquely defined for each axon. Mathematically, this can be described as:

$$\text{Affine:} \quad T < T_1$$

$$\text{Non-affine:} \quad T > T_2$$

$$\text{Switching:} \quad T_1 \leq T \leq T_2$$

where T is the current tortuosity of the axon, and T_1 and T_2 are bounds that describe a uniform distribution from which the transition tortuosity (T_t) for an axon is randomly assigned. Under these conditions, a highly tortuous axon with tortuosity $T > T_t$ will follow non-affine behavior. As the tissue-level stretch increases, the axon straightens until the tortuosity reaches the transition tortuosity, when its behavior switches to affine.

Using this scheme, the bounds of the uniform distribution that describes the transition tortuosity can be interpreted as a measure of the propensity for affine or non-affine behavior. For each developmental stage, a Levenberg–Marquardt multi-parameter, nonlinear regression scheme was employed to adjust these bounds to minimize net differences between experimental and predicted histograms across all stretch levels. The model was executed 100 times for each case, from which the mean values, standard deviation, and regression coefficients for each fit were determined. In our previous study, the fitting procedure uniformly resulted in the lower bound $T_1 < 1$ and the upper bound $T_2 > 1$. With these conditions, a fraction of the transition tortuosities $[(1 - T_1)/(T_2 - T_1)]$ will be less than 1. For this fraction of axons, because the minimum value for actual tortuosity is 1, the transition tortuosity is never reached, and the axons will exhibit non-affine behavior permanently.

2.7 Equation validation

Finite element analysis (FEA) was used to validate the 3-D kinematic model equations. These models were developed using the ABAQUS software suite (Simulia). A population of seven axons (Stiffness, $E = 0.29\,\text{kPa}$, Poisson's Ratio, $\nu = 0.49$, Density, $\rho = 1250\,\text{kg/m}^3$; Magdesian et al. 2012; Ouyang et al. 2013), with varying tortuosities was

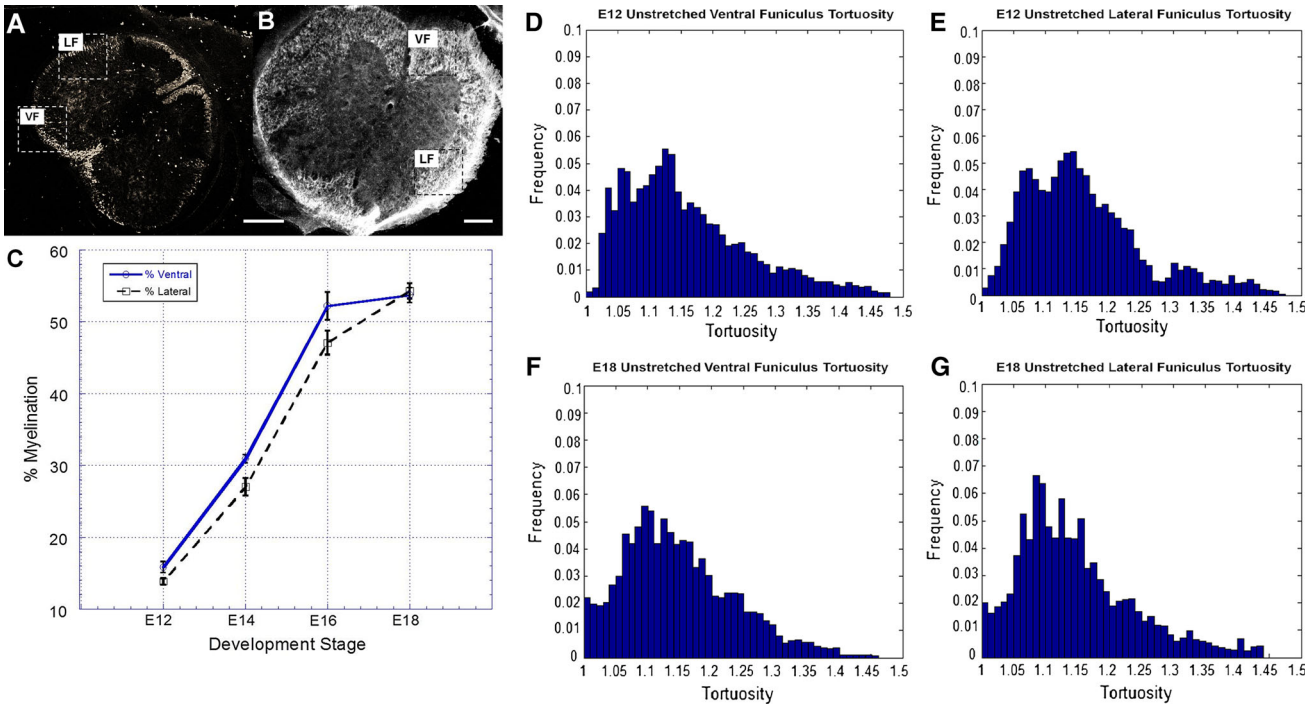

Fig. 2 **a** Representative image of neurofilament and MBP immunolabeled **a** E12, and **b** E18 spinal cord transverse section. (*scale bar* = 200 μm). Axons were characterized in the ventral funiculus (VF) and lateral funiculus (LF). **c** Percentage of myelinated fibers in unstretched spinal cords at each development stage ($N = 3$ cords). Myelinated axons were counted in osmium tetroxide-stained sections. *Error bars* = standard error of the mean. **d, e** Histograms for 3-D tortuosity for ventral funiculus ($N = 887$) and lateral funiculus ($N = 775$) for E12 unstretched cords, and **f, g** E18 unstretched cords. No statistical significance was seen between ventral and lateral distributions at E12 ($P = 0.087$), E18 ($P = 0.092$), or for any other development stages ($P_{\min} = 0.081$)

generated. A MATLAB script was employed to extract the nodal positions and calculate the original and final tortuosities. Non-affine axons were modeled as single helical coils and stretched either 10 or 20 % of the original end-to-end length. Affine axons were modeled as the same helical coils embedded in a solid matrix. Tie constraints were incorporated between axons and the surrounding matrix to simulate complete coupling. The 10 or 20 % stretch was then applied to the solid matrix.

3 Results

3.1 Growth and morphological features of spinal cords

Figure 2a, b shows representative images of stained transverse sections of spinal cords from E12 and E18, respectively. The average length of the spinal cord increased from 14.7 ± 1.6 mm at E12 ($N = 22$) to 24.2 ± 2.8 mm at E18 ($N = 24$), similar to results from our previous study. Lengths of the semi-major axis for spinal cord cross sections increased from 884 ± 122 μm at E12 to 2290 ± 274 μm at E18.

We determined the percentage of myelinated fibers at each development stage for both the lateral funiculus and ventral funiculus (Fig. 2c). More myelinated fibers were found in the ventral funiculus from E12 to E16. At E18, the percentages of myelinated fibers are equal in both regions. This trend is consistent with previous findings (Chung K 1983). Myelination followed a sigmoidal relationship in both regions, where the largest increase was seen between E14 and E16. We also examined the G-ratio, which is a measure of the amount of myelin around an axon. Differences in the G-ratio between the ventral and lateral funiculus for each stage of development were evaluated with a Kruskal–Wallis (K–W) nonparametric test and were not statistically significant ($P_{\min} = 0.227$).

Distributions of axon tortuosity in the lateral and ventral funiculus were compared at 0 % and at 10 % stretch at each developmental stage. Histograms of 3-D axon tortuosity for unstretched E12 and E18 specimens at each region are shown in Fig. 2d–g. The only statistically significant difference between the two regions was observed in E14 spinal cords exposed to 10 % stretch ($P = 0.049$, data not shown). Tortuosity significantly decreased as stretch level increased.

3.2 2-D and 3-D tortuosity measures

Mean 3-D tortuosity decreased with increasing stretch for each developmental stage. For example, in E18 specimens, tortuosity decreased from 1.146 to 1.042 as stretch increased

from 0 to 20 %. The largest decrease in average tortuosity was observed in E12 samples (1.158–1.018). K–W tests were used to evaluate the differences between the x–z and y–z tortuosities extracted from confocal stacks of transverse sections and 2-D tortuosities measured by hand from longitudinal sections. No statistical significance was found in either x–z or y–z orientations ($P_{\min} = 0.094$), and these data were subsequently combined for our microkinematic analyses.

Mean 3-D tortuosity was consistently higher than 2-D for all given development and stretch levels (Fig. 3a). For both 2-D and 3-D cases, tortuosity of unstretched samples decreased with development, but increased with development at higher stretch levels. Tortuosity was also compared across the three regions of the spinal cord. Two-tailed K–W tests were done among the distributions generated for the cervical (C3–C8), thoracic (C8–T4), and lumbar regions (T5–L4) at each age and stretch level. No statistically significant differences were found ($P_{\min} = 0.071$), and the regional distributions were pooled into a single distribution per age group and stretch level.

The distributions of tortuosity with stretch (Fig. 3b) demonstrate some important trends. For example, in all age groups, axons are the straightest at the highest stretch level. However, the percentage of axons that can be classified as "perfectly straight" decreases with increasing age, which indicates a shift to affine kinematics with development and myelination. In particular, a significant drop in straight axons was observed from E14 to E16, where the percentage of perfectly straight axons fell from 50 % to 35 %. We compared distributions across development stages for a given stretch using pairwise, two-tailed Kolmogorov-Smirnov (K-S) tests ($P < 0.01$) and found significant changes in the tortuosity distribution in control samples ($P_{\max} = 0.004$), 10 % stretch level ($P_{\max} = 0.001$), and 20 % stretch level ($P_{\max} < 0.001$).

3.3 Microkinematic behavior

We extended previously developed models to characterize the 3-D microkinematic behavior for axons. At each developmental stage, distributions for unstretched axons were used as the input data. The kinematic models were used to predict the response assuming pure affine and non-affine behaviors. These idealized models were first validated against a finite element model. The kinematic model results and finite element simulations agreed to within 0.6 % axon stretch (or 3.4 % engineering strain) (Table 1). To determine the switching behavior, the bounds of the transition tortuosity distribution, T_1, and T_2 were computationally iterated to allow an axon to move from non-affine to affine behavior until the predicted tortuosity distributions at the four different stretch levels converged against the experimental distributions.

Using our unstretched tortuosity data as input, we calculated "idealized" distributions of tortuosity at different stretch levels when axons exhibit pure affine and non-affine behaviors. Neither the pure affine nor non-affine models matched the experimental data for a given tissue-level stretch at any developmental stage ("Appendix" Fig. 6). Allowing axons to transition from non-affine to affine kinematics according to the switching model improved the agreement between the model results and experimental data, based on K–W test statistics ($P < 0.001$). Similar to the 2-D study, we found that more developed spinal cords showed more affine-like behavior. For example, there was an 11 % decrease in the percentage of perfectly straight axons from E12 profile to E18 at 10 % stretch. As shown in Fig. 4a, T_1 increased with developmental stage, whereas T_2 values remained relatively constant. This trend was also seen in 2-D distributions, though no statistically significant differences were found between 2-D and 3-D lower bound (T_1) transition parameters ($P_{\min} = 0.114$). These values were used to estimate the percentage of axons that follow purely non-affine kinematics. As shown in Fig. 4c, the percentage of axons predicted to behave purely non-affinely decreased during development from ∼50 % at E12 to ∼20 % at E18. The predicted percentage of non-affine axons was also consistently lower from the 3-D data than from the 2-D data at all developmental stages ($P < 0.005$).

4 Discussion

In this study, we present a quantitative characterization of CNS axon tortuosity in 3-D using a novel image processing algorithm to extract axon positions from confocal images of spinal cord cross sections. Using a nearest-neighbor methodology, we tracked single axon pathways through cross sections of spinal cord slices. The algorithm finds axons and measures the displacement of their center points to determine tortuosity. We also stained for myelin basic protein as an indicator of spinal cord myelination, as well as to ensure that our characterizations targeted white matter axons. There was excellent agreement between 2-D data extracted from the 3-D characterization of transverse cross sections and the 2-D data previously acquired from longitudinal slices (Hao and Shreiber 2007) and from longitudinal sections processed in parallel in this study, which validated our image processing algorithm.

We then used tortuosity as a metric to evaluate axonal kinematics during controlled stretch of white matter. We found that our results in 3-D follow the same general kinematic trends as those found in 2-D with some consistent differences in the magnitude of the response. Previously, we estimated an 8.3 % increase in tortuosity in unstretched axons by projecting 2-D results to 3-D by assuming that an axon resembles a coil with amplitude that is 10 % of the axon's periodic-

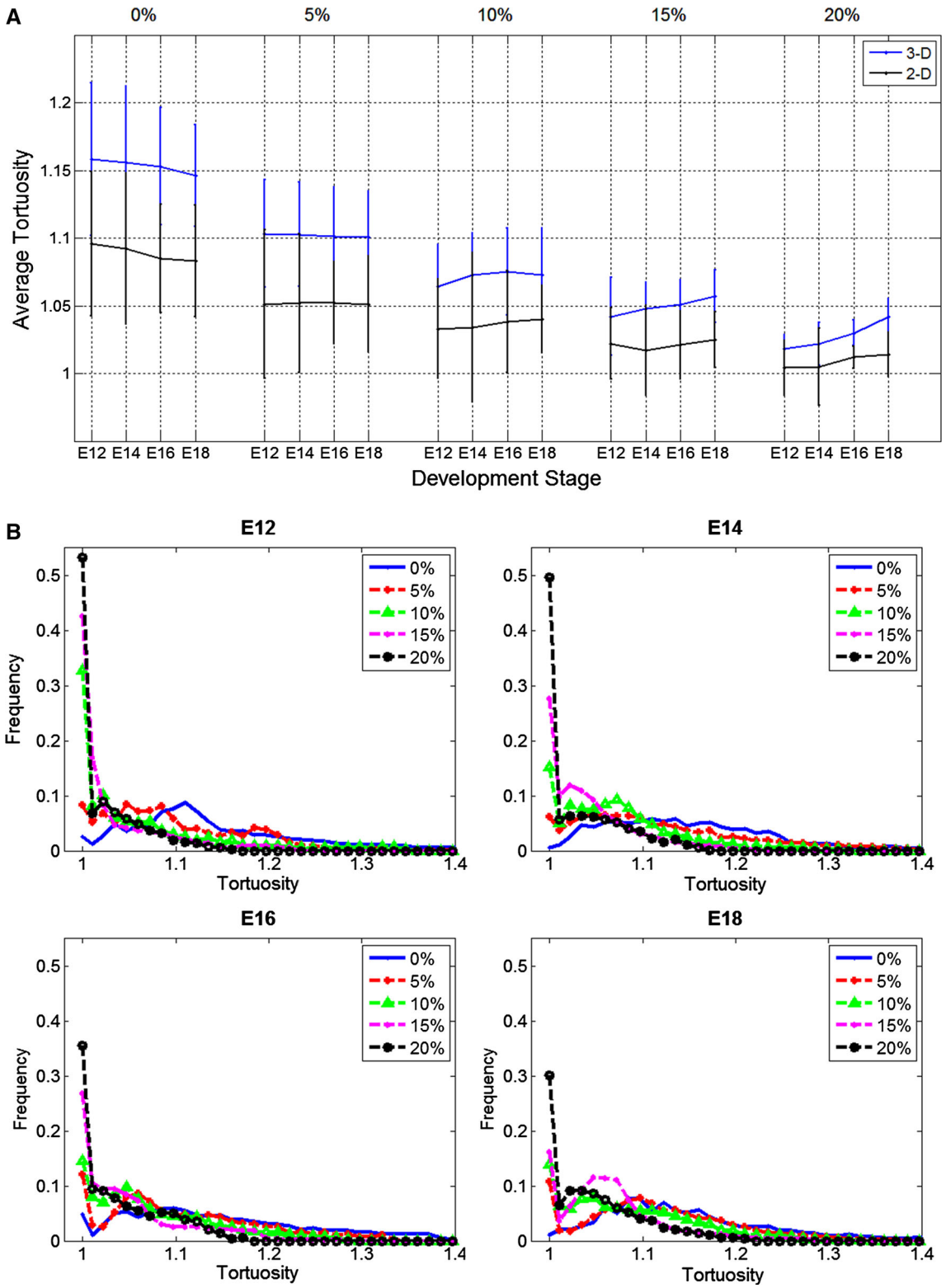

Fig. 3 **a** Mean 3-D and 2-D tortuosity decreases with stretch level. 2-D tortuosity was extracted from tracings made from longitudinal slices of spinal cord. Similar trends are observed in the 2-D and 3-D case: (1) Average tortuosity decreases with stretch; (2) In unstretched tissue, tortuosity decreases with development. However, as stretch increases, the trend reverses and tortuosity increases with development. *Error bars* = standard deviation. **b** Normalized frequency distributions for 3-D tortuosity for each chick embryo development stage. As the spinal cord embryo develops, there is a shift toward affine behavior, demonstrated by the decrease in perfectly straight axons from ~55 % at E12 to ~30 % at E18

Table 1 Results from FEM for axons (N=7) modeled with varying initial tortuosities

Stretch level (%)	Initial Tortuosity				Predicted tortuosity following stretch							
					Affine				Non-affine			
	Equation		Model		Equation		Model		Equation		Model	
	Mean	SD	Mean	SD	Mean	SD	Mean	SD	Mean	SD	Mean	SD
10 %	1.148	0.074	1.148	0.074	1.108	0.042	1.109	0.048	1.044	0.039	1.046	0.038
15 %	1.148	0.074	1.148	0.074	1.097	0.037	1.100	0.035	1.000	0.012	1.000	0.011
20 %	1.148	0.074	1.148	0.074	1.086	0.025	1.085	0.036	1.000	0.006	1.000	0.009

Axons were either completely tied (Affine) to surrounding matrix or untied (Non-affine). Equation and model values for stretch agreed within 0.6 %

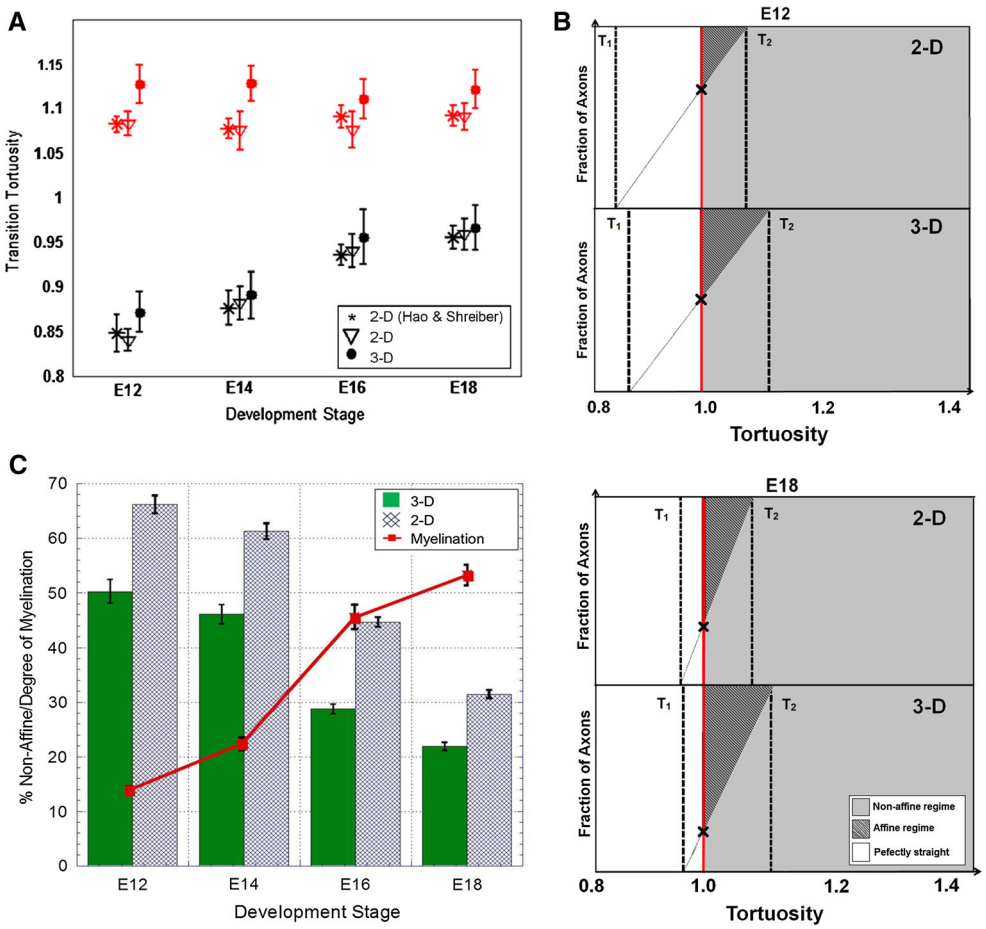

Fig. 4 Transition tortuosity results and interpretation. **a** *Lower* (T_1, *black*) and *upper* (T_2, *red*) bound transition tortuosity as a function of development stage. T_1 consistently increased with age. T_2 remained roughly constant with development stage in both 2-D and 3-D. However, T_2 values for 3-D distributions were consistently higher than 2-D. **b** Graphical representation of non-affine (*grey*) and affine regimes (*hashed*) of 2-D and 3-D axons for E12 and E18. The *bold dashed lines* correspond to the transition parameters from Fig. 4a. The diagonal line corresponds to the cumulative uniform distribution on the interval $[T_1, T_2]$ of switching tortuosities. The intersection of the uniform distribution and the line $T = 1$ (*red line*) is marked with an X and represents the percentage of axons that are predicted to permanently exhibit non-affine kinematics. The values of T_1 and T_2 dictate this percentage. The increase in T_1 from E12 to E18 shifts the intercept down, which corresponds to an increase in affine behavior. The increase in T_2 from the 2-D characterization to the 3-D characterization also shifts the intercept down and indicates more affine behavior. **c** Predicted percentage of purely non-affine axons as a function of development stage. Myelination also increases with development, with the biggest drop in non-affine axons coinciding with the greatest increase in myelination between E14 and E16 (*Error bars* = standard error of mean)

ity (Hao and Shreiber 2007). This predicted increase in the path length of the axon is consistent with our more direct comparison in this work, where the average tortuosity in unstretched samples was 5.3 % greater when measured in 3-D vs. 2-D. The 3-D tortuosity of axons within unstretched tissue decreased with development stage for the chick spinal cord, with axons becoming straighter with age and growth, and also decreased after the tissue was exposed to quasistatic stretch. When the 3-D tortuosity data across all developmental stages and stretch levels are considered, similar trends to our previous 2-D characterization were observed, where mean tortuosity demonstrates a downward trend with development stage at low stretch levels, which reverses at higher levels of stretch (Fig. 3a) (Hao and Shreiber 2007).

As a result of physical growth of the spinal cord, the tortuosity of unstretched axons decreased with increasing development. The axial length of the spinal cord increased with development by almost 104 % between E12 and E18 specimens, with a large spurt in growth seen between E12–E14 and E14–E16 (∼23 % increase between each period), and the diameter doubled in the same timeframe. This growth-induced tension may be responsible for the increase in the proportion of axons with a tortuosity of 1 during development. Results of the kinematic characterization in 3-D were similar to those found in the 2-D characterization (Hao and Shreiber 2007; Bain et al. 2003). These previous studies implied that the kinematic transition from non-affine to affine behavior is primarily driven by the interconnections among axons via myelination, and not natural straightening of axons due to growth-induced tension.

Axons in 3-D followed a model that allows transition from non-affine to affine kinematics. In general, the value of the lower (T_1) and upper (T_2) bounds of the transition tortuosity distribution were larger for the 3-D characterization than the 2-D (Fig. 4a). However, these differences were consistently significant only for the upper bound across embryonic stages ($P_{\max} = 0.037$ for E16). Figure 4b provides a graphical interpretation of the transition tortuosity results. An axon initially behaves with non-affine kinematics as it is stretched until its tortuoisty reaches T_2. From this point, the probability that the axon switches to affine kinematics is based on a uniform distribution with lower bound T_1 and upper bound T_2. Thus, when a population of axons is considered, the intercept of the sloped line from this distribution with the line $T = 1$ (red line in Fig. 4b) represents the fraction of axons which are predicted to exhibit purely non-affine kinematics regardless of stretch because the actual tortuosity cannot decrease below 1. Lower values of T_1 and of T_2 will decrease the percentage of non-affine axons. Therefore, as development progresses from E12 to E18 and T_1 increases in value while T_2 remains constant, the intercept increases, which implies that a smaller proportion of axons will remain permanently non-affine. Figure 4b also demonstrates how the larger T_2 value for 3-D vs. 2-D behavior indicates a propensity for more affine behavior. Figure 4c depicts the percentage of permanently non-affine axons as a function of development stage. As with our previous 2-D study, this percentage decreased with development stage, falling about 31 % from E12-E18 compared to 34 % from our previous 2-D results (Hao and Shreiber 2007). Collectively, these results support the hypothesis that increased myelination and glial presence is linked to coupling behavior and that these features influence 3-D kinematic behavior in a similar fashion to 2-D.

We characterized both the ventral and lateral funiculus regions of the spinal cord. In preliminary experiments, we observed the highest amount of immunofluorescence and best image quality in the ventral funiculus. We also examined the lateral funiculus to provide direct comparisons to our previous study (Hao and Shreiber 2007). We found that tortuosity is similar in both regions, but the profile of myelination during development was different particularly at E14, where more myelinated fibers were present in the ventral funiculus. This generally agrees with previous studies that identified the ventral funiculus as one of the first to myelinate (Anderson et al. 2000). When the tortuosity data for the two regions were fit to our kinematic model, more affine-like behavior was predicted for the ventral funiculus than the lateral funiculus, which supports the role myelin plays in inducing kinematic coupling behavior. By E18, myelination in the ventral and lateral funiculi was not significantly different.

We modeled axons using sinusoidal parametric equations, enabling us to construct an analytical solution for describing how axon tortuosity changes with stretch in the affine case. Our models used a cross-ratio of amplitude-to-periodicity ('k') of 1 in calculations. Our 2-D characterizations showed amplitude and periodicity was independent of axon orientation in the spinal cord, justifying our selection of $k = 1$.

Our results here and in our previous study (Hao and Shreiber 2007) may influence axonal injury thresholds. Under a non-affine framework, we assume that the microstructure does not experience strain until the axon has unfolded and fully straightened, contrasting with affine kinematics, in which strain is immediately transferred to axons with tissue-level stretch. The higher tortuosities observed in 3-D versus 2-D suggest that axons exhibiting purely non-affine kinematics have a greater threshold of macroscopic stretch than axons that switch or are already behaving with affine kinematics. When we examine this in the context of switching kinematics, our T_2 parameter increases by 3.7 % when comparing 2-D and 3-D, which is less than the increase in mean tortuosity, suggesting that macroscopic injury thresholds when the 3-D path is accounted for will be greater at earlier stages of development where a larger proportion of axons are non-affine.

Although this characterization of axon kinematics is in 3-D, the consistency of the results and trends between 2-D and 3-D and between two different tissue types and

species (developing chick spinal cord and adult guinea pig optic nerve) (Bain et al. 2003), especially for "fully myelinated" tissue suggests that the approach can be incorporated into computational models of traumatic brain injury and spinal cord injury. This may be best accomplished using a multi-scale framework that employs representative volume elements of white matter (Cloots et al. 2011; Karami et al. 2009; Pan et al. 2011, 2013). Multi-scale models have the potential to capture the evolution of anisotropic tissue properties as the microstructure mechanically responds to applied loads. These models may also translate the macroscale response to the microscale, where individual entities can be explicitly defined, to predict injury to individual cellular or tissue components. For axonal injury, this latter aspect is particularly important, given the large discrepancy between strain injury thresholds determined from in vivo models at the tissue level (Bain and Meaney 2000) and those found from in vitro preparations of individual axons (Smith et al. 1999; Tang-Schomer et al. 2010; Wright and Ramesh 2012).

We have previously developed RVEs based on the "switching" kinematic framework described herein that have accurately predicted the evolution of tortuosity with stretch and the resultant tissue-level mechanical properties for axial loading of spinal cord tissue (Pan et al. 2013). For this RVE approach to be adopted for models of brain injury, however, the tortuosity of different regions of white matter must be characterized, which is a burdensome and difficult chore. Rapid advances in imaging techniques may enable noninvasive determination of white matter microstructure. For example, diffusion tensor imaging (DTI) is a potential method for characterizing both the tortuosity and the myelination of axons. Nilsson et al. modeled water diffusion within undulated axons and concluded that the tortuosity increases the diffusion time parameter to the equivalent of doubling axon diameter, confining the space in which water molecules can diffuse (Nilsson et al. 2012). Their study also represented axons as helical coils. Although the axon path can be modeled as a persistent random walk (Katz 1985), which may more closely resemble the actual path, the regular geometry associated with the helical coil model enabled an analytical solution for the affine kinematic behavior and simplified modeling of diffusion as well. Stochasticity can then be introduced to a population of axons. Our models used a cross-ratio of amplitude-to-periodicity ('k') of 1 in calculations. The cross-ratio can be adjusted to account for differences in axon morphology in different regions of white matter. Our focus on oriented white matter in the spinal cord simplified the analysis of axon kinematics. However, axon orientation is an important feature that models should capture, as it varies in different regions of CNS, conferring isotropy in some regions, and anisotropy in others. It is clear that axon orientation influences strains experienced by these microstructural elements. Cloots et al. reported that maximum axonal strain relative to applied stress was modeled to occur when the tissue-loading direction is 45° of the main axonal direction (Cloots et al. 2011), though the study omits the effects of undulation and kinematic behavior. Studies on randomly oriented collagen fiber networks showed that both orientation and kinematics influenced the strains experienced by individual fibers (Chandran and Barocas 2006). Axon orientation would particularly influence straightening and rotation of non-affine axons if, for example, the direction of tissue-level stretch was parallel to the axon's main orientation. Other work highlights experimental differences in straight vs. undulated axon fibers (Assaf et al. 2000), and in myelinated vs. unmyelinated fibers (Kunz et al. 2014). Extracting such information would allow development of RVEs for many in vivo models of TBI as well as simulations of clinical cases of TBI.

Acknowledgments Funding for this study was provided by the NSF CMMI Grant #1000450.

Appendix

The equations that describe the non-affine and affine kinematics of axons in 3-D are extensions of the 2-D descriptions (Bain and Meaney 2000; Hao and Shreiber 2007). In both cases, our goal was to derive an equation for axon tortuosity as a function of tissue-level stretch ratio, λ and the original tortuosity, T_0.

Non-affine behavior

In 2-D, the microstructural transformation was calculated from the initial tortuosity and macroscopic stretch ratio:

$$T_{2D} = \frac{1}{\lambda} T_0 \quad \text{for } \lambda < T_0 \tag{4}$$

When the stretch ratio equals the initial tortuosity, the axon has completely straightened. If the stretch ratio continues to increase, the axon begins to stretch, but remains completely straight; mathematically, this can be expressed as:

$$T_{2D} = 1 \quad \text{for } \lambda \geq T_0 \tag{5}$$

The same transformation applies for non-affine kinematics in 3-D; axons when uncoupled will straighten according to the level of stretch, regardless of the additional plane of undulation. Mathematically, this can be written as:

$$T_{3D} = \frac{1}{\lambda} T_0 \quad \text{for } \lambda < T_0 \tag{1}$$

$$T_{3D} = 1 \quad \text{for } \lambda \geq T_0 \tag{2}$$

Equations (1) and (2) can be found in the body of the text.

Affine behavior

In 2-D, the undulated axon was modeled as a cosine wave with amplitude A_0 and period P_0 where the tortuosity of the 2-D axon, T_{2D} of the stretched axon from 0 to its end-to-end length, L_E could be calculated:

$$T_{2D} = \frac{1}{L_E}\int_0^{L_E}\sqrt{1+\left(\left(\frac{-A_0}{\sqrt{\lambda}}\right)\left(\frac{2\pi}{\lambda T_0}\right)\sin\left(\frac{2\pi z}{\lambda T_0}\right)\right)^2}\,dz \tag{6}$$

There is no closed form solution for (6). A solution was approximated using a simplification applicable for tortuosity values close to 1, producing the following transformation linking initial tortuosity and stretch ratio for 2-dimensional axons under an affine regime (Bain et al. 2003):

$$T_{2D} = T_0\left[\frac{1}{\lambda^3}+\frac{1}{T_0^2}\left(1-\frac{1}{\lambda^3}\right)\right]^{1/2} \tag{7}$$

To adapt this approach for 3-dimensional kinematics, the 3-D axon is modeled as a helical coil, using two parametric periodic functions to describe the undeformed axon's path in each plane:

$$y(z) = A_{yz}\cos\left(\frac{2\pi z}{P_{yz}}\right)\quad \frac{dy(z)}{dz} = -\frac{2\pi A_{yz}}{P_{yz}}\sin\left(\frac{2\pi z}{P_{yz}}\right) \tag{8}$$

$$x(z) = A_{xz}\sin\left(\frac{2\pi z}{P_{xz}}\right)\quad \frac{dx(z)}{dz} = \frac{2\pi A_{xz}}{P_{xz}}\cos\left(\frac{2\pi z}{P_{xz}}\right) \tag{9}$$

First, the initial tortuosity is expressed as a function of the undeformed pathlength. The pathlength is found from the differentiated forms of (8) and (9) and integrating the incremental path of the axon along the end-to-end length L_e, which is divided by the end-to-end length to generate an expression for initial tortuosity:

$$T_0 = \frac{1}{L_e}\int_0^{L_e}\sqrt{1+\left(-\frac{2\pi A_{yz}}{P_{yz}}\sin\left(\frac{2\pi z}{P_{yz}}\right)\right)^2+\left(\frac{2\pi A_{xz}}{P_{xz}}\cos\left(\frac{2\pi z}{P_{xz}}\right)\right)^2}\,dz \tag{10}$$

Similar to (6), this integral does not have an analytical solution. The solution can be approximated by using the formula for the arc length of a helical coil:

$$s = 2\pi\sqrt{r^2+C_0^2} \tag{11}$$

where s is the arc length, r is the average radius of the helix, and C_0 is the helix pitch. The periodicity was assumed to be constant along the axis. The end-to-end length for one period of the helical axon was assumed to be $2\pi P_{yz}P_{xz}$. With these assumptions, Eq. (11) can be rewritten as:

$$s = 2\pi\sqrt{\frac{1}{4}(A_{xz}+A_{yz})^2+1^2} \tag{12}$$

Dividing (12) by the end-to-end length yields the initial tortuosity of the 3-D helical axon:

$$T_0 = \sqrt{1+\frac{(A_{yz}^2+A_{xz}^2)}{4}+2\pi\left(\frac{A_{yz}}{P_{xz}}\frac{A_{xz}}{P_{yz}}\right)} \tag{13}$$

To simplify (13), we denote the cross-ratio, $(A_{yz}/P_{xz} = A_{xz}/P_{yz})$ as a single variable, k. Thus, (13) becomes:

$$T_0 = \sqrt{1+\frac{(A_{yz}^2+A_{xz}^2)}{4}+2\pi k^2} \tag{14}$$

The next step is to derive an expression for the pathlength of the deformed axon. By assuming incompressibility and isotropy, the axon's amplitude and periodicity after deformation to a given stretch ratio is:

$$\begin{aligned} A_{xz,\text{stretched}} &= A_{xz}\left(\lambda^{-\frac{1}{3}}\right)\quad A_{yz,\text{stretched}} = A_{yz}\left(\lambda^{-\frac{1}{3}}\right)\\ P_{xz,\text{stretched}} &= P_{xz}(\lambda)\quad P_{yz,\text{stretched}} = P_{yz}(\lambda)\end{aligned} \tag{15}$$

Employing the same approach as in the case of the undeformed axon [the resultant pathlength integral cannot be analytically solved as was the case in (6) and (10)], the equation for the arc length of a helical coil was adapted for the deformed case:

$$s = 2\pi\sqrt{\frac{1}{4}\left(\frac{A_{xz}}{\sqrt[3]{\lambda}}\right)^2+\left(\frac{A_{yz}}{\sqrt[3]{\lambda}}\right)^2+\left(\frac{2A_{xz}A_{yz}}{\lambda^{2/3}}\right)+1} \tag{16}$$

The deformed end-to-end length is:

$$L_E = 2\lambda^2 P_{xz}P_{yz} \tag{17}$$

Dividing (16) by (17) and substituting in (14) gives the equation which links the transformed tortuosity to initial tortuosity and macroscopic stretch for axons in 3-D exhibiting affine behavior [Eq. (3) in the main text] (Figs. 5, 6).

$$T_{3D} = T_0\sqrt{\left\{\frac{1}{\lambda^{8/3}}+\frac{1}{T_0^2}\left[1-\frac{2\pi}{(2\pi+k^2)\,\lambda^{8/3}}\left(\frac{1}{k^2}+\frac{1}{2\pi}\right)\right]\right\}} \tag{3}$$

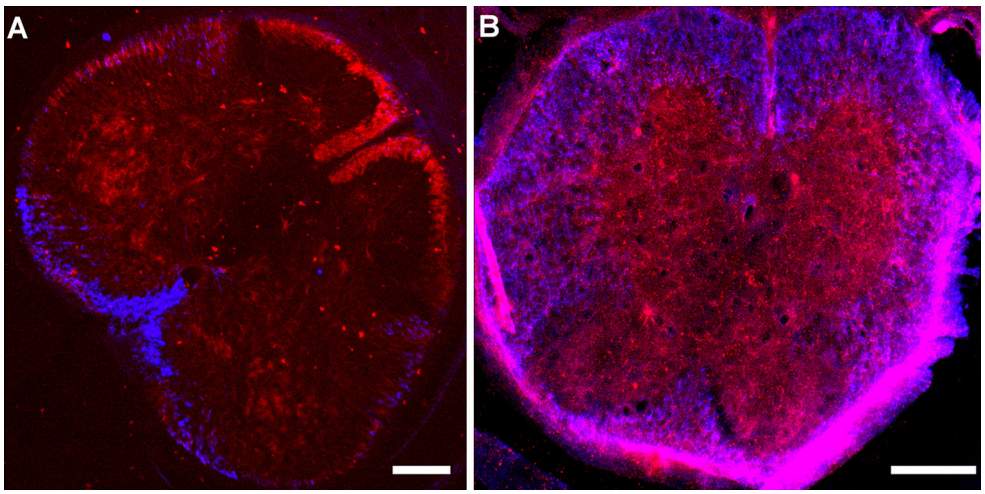

Fig. 5 Pseudo-colored images of transverse sections to distinguish neurofilament (*red*) from Myelin Basic Protein (*blue*) for **a** E12 (*scale bar* = 100 μm), and **b** E18 (*scale bar* = 200 μm)

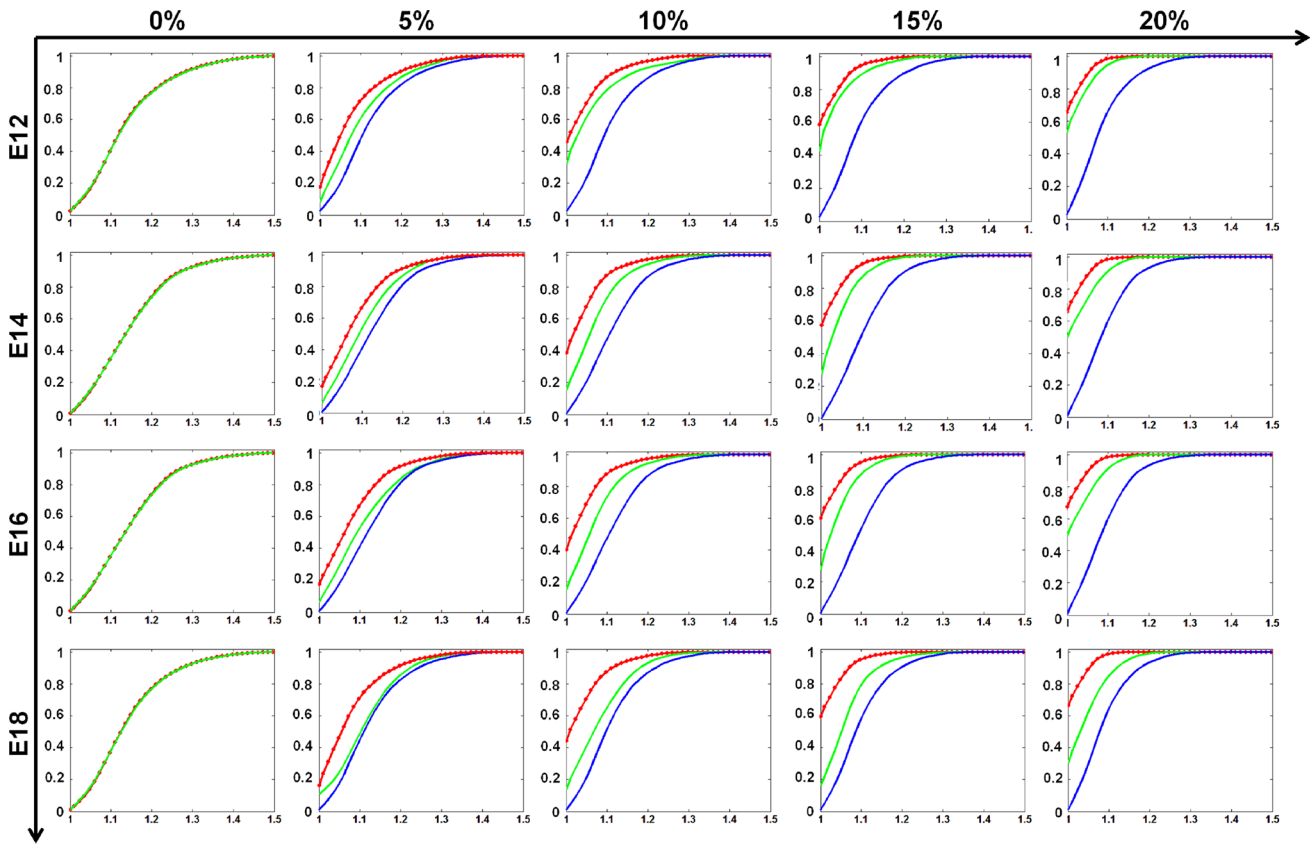

Fig. 6 Cumulative Frequency Distribution plots of 3-D axon tortuosity for experimentally characterized distribution of axons (*green*), axons predicted to behave ideally non-affine (*red*), and axons predicted to behave ideally affine (*blue*) at different stretch levels and stages of development. There is a trend for the experimental distribution to move closer to the idealized affine curve with age for a given stretch level. In all cases, neither idealized distribution fits the experimental distribution perfectly. Average goodness of fit was 0.842

References

Anderson ES, Bjartmar C, Hildebrand C (2000) Myelination of prospective large fibres in chicken ventral funiculus. J Neurocytol 29(10):755–764

Assaf Y, Mayk A, Cohen Y (2000) Displacement imaging of spinal cord using q-space diffusion weighted MRI. Magn Reson Med 722:713–722

Bain A, Meaney D (2000) Tissue-level thresholds for axonal damage in an experimental model of central nervous system white matter injury. J Biomech Eng 122(December):615–622

Bain AC, Shreiber DI, Meaney DF (2003) Modeling of microstructural kinematics during simple elongation of central nervous system tissue. J Biomech Eng 125(6):798

Bas E, Erdogmus D (2010) Piecewise linear cylinder models for 3-dimensional axon segmentation in brainbow imagery. From Nano to Macro., Biomedical Imaging, pp 1297–1300

Chandran PL, Barocas VH (2006) Affine versus non-affine fibril kinematics in collagen networks: theoretical studies of network behavior. J Biomech Eng 128(2):259–270

Chomiak T, Hu B (2009) What is the optimal value of the g-ratio for myelinated fibers in the rat CNS? A theoretical approach. PloS one 4(11):e7754

Chung K CR (1983) Numbers of axons in lateral and ventral funiculi of rat sacral spinal cord. J Comp Neurol 10(214):72–78

Cloots RJH et al (2011) Micromechanics of diffuse axonal injury: influence of axonal orientation and anisotropy. Biomech Model Mechanobiol 10(3):413–422

Hao H, Shreiber DI (2007) Axon kinematics change during growth and development. J Biomech Eng 129(4):511–522

Karami G et al (2009) A micromechanical hyperelastic modeling of brain white matter under large deformation. J Mech Behav Biomed Mater 2(3):243–254

Katz MJ (1985) How straight do axons grow? J Neurosci off J Soc Neurosci 5(3):589–595

Kunz N et al (2014) Assessing white matter microstructure of the newborn with multi-shell diffusion MRI and biophysical compartment models. NeuroImage 96:288–299

Magdesian MH et al (2012) Atomic force microscopy reveals important differences in axonal resistance to injury. Biophys J 103(3):405–414

Nilsson M et al (2012) The importance of axonal undulation in diffusion MR measurements: a Monte Carlo simulation study. NMR Biomed 25(5):795–805

Ouyang H, Nauman E, Shi R (2013) Contribution of cytoskeletal elements to the axonal mechanical properties. J Biol Eng 7(1):21

Pan Y et al (2013) Finite element modeling of CNS white matter kinematics: use of a 3D RVE to determine material properties. Front Bioeng Biotechnol 1(December):1–10

Pan Y, Shreiber DI, Pelegri AA (2011) A transition model for finite element simulation of kinematics of central nervous system white matter. IEEE Trans Bio-med Eng 58(12):3443–3446

Shreiber DI, Hao H, Elias RA (2009) Probing the influence of myelin and glia on the tensile properties of the spinal cord. Biomech Model Mechanobiol 8(4):311–321

Smith DH et al (1999) High tolerance and delayed elastic response of cultured axons to dynamic stretch injury. J Neurosci Off J Soc Neurosci 19(11):4263–4269

Smith DH, Meaney DF (2000) Axonal damage in traumatic brain injury. Neurosci 6(6):483–495

Tang-Schomer MD et al (2010) Mechanical breaking of microtubules in axons during dynamic stretch injury underlies delayed elasticity, microtubule disassembly, and axon degeneration. FASEB J 24(5):1401–1410

Wright RM, Ramesh KT (2012) An axonal strain injury criterion for traumatic brain injury. Biomech Model Mechanobiol 11(1–2):245–260